A numerical study of a size-dependent finite-element based unit cell with primary and secondary voids

Vetle Espeseth [a,*], David Morin [a,b], Jonas Faleskog [c], Tore Børvik [a,b], Odd Sture Hopperstad [a,b]

[a] *Structural Impact Laboratory (SIMLab), Department of Structural Engineering, NTNU – Norwegian University of Science and Technology, Trondheim, Norway*
[b] *Centre for Advanced Structural Analysis, NTNU, Trondheim, Norway*
[c] *Solid Mechanics, Department of Engineering Mechanics, KTH Royal Institute of Technology, Stockholm, Sweden*

ARTICLE INFO

ABSTRACT

Aluminium alloys contain various types of intermetallic particles with different sizes, such as constituent particles and dispersoids. The main mechanism of ductile fracture in these materials is assumed to be nucleation of voids around the constituent particles, which grow during plastic deformation and eventually coalesce, resulting in material failure. The role of the dispersoids is less certain, but they are assumed to contribute in the last stages of the ductile fracture process. While the constituent particles are in the range of a couple of microns, the size of dispersoids is normally one order of magnitude smaller. To disclose the possible effects of the dispersoids on the ductile fracture process in aluminium alloys, this paper presents a numerical study of a finite-element based unit cell, which consists of a single spherical void embedded in a matrix material represented by a porous plasticity model with void size effects. Accordingly, the single, primary void of the unit cell is assumed to have nucleated on a constituent particle, whereas the matrix porosity is assumed to account for secondary, smaller voids nucleated on dispersoids. The effects of the intrinsic length scale of the matrix material on the void growth and coalescence are studied for a range of stress states, while the initial primary and secondary void volume fractions are kept constant. The secondary voids have a substantial effect on the behaviour of the unit cell when their size is large compared to the intrinsic material length scale, but they were not found to influence the growth of the primary void. Instead, the growth of the secondary voids promotes strain softening and influences the coalescence process of the primary voids, which gradually changes mode from internal necking to loss of load-carrying capacity of the inter-void ligament.

1. Introduction

The failure processes in ductile materials are governed by the nucleation of voids at small second-phase particles and subsequent growth and coalescence of these microscopic cavities (Benzerga and Leblond, 2010). Nucleation occurs either through decohesion between the matrix material and the particles or by cracking of particles when the stress at the surface is sufficient (Maire et al., 2011; Westermann et al., 2014; Pedersen et al., 2015; Pineau et al., 2016). Microscopic voids may also be present in the material before

---

* Corresponding author.
E-mail address: vetle.espeseth@ntnu.no (V. Espeseth).

deformation (Campbell, 2011; Toda et al., 2014). Voids will continue to grow under plastic deformation until they eventually coalesce and result in material failure. The stress state is recognized as one of the main factors influencing the fracture strain of a given material subjected to plastic deformation. McClintock (1968) and Rice and Tracey (1969) were among the first to address the importance of the stress triaxiality on the growth phase. While the effects of the stress triaxiality are well established (Needleman and Tvergaard, 1984; Johnson and Cook, 1985; Mirza et al., 1996; Alves and Jones, 1999; El-Magd and Brodmann, 2001; Westermann et al., 2014), more recent studies acknowledge the importance of the deviatoric stress state on the damage evolution in ductile materials (Bao and Wierzbicki, 2004; Barsoum and Faleskog, 2007, 2011; Gao et al., 2009; Dunand and Mohr, 2011; Gruben et al., 2012; Faleskog and Barsoum, 2013; Haltom et al., 2013; Scales et al., 2016; Erice et al., 2018), particularly at low stress triaxialities. Whereas intermediate to high stress triaxialities result in large dimples on the fracture surface due to void growth and internal necking of the inter-void ligament, elongated small shear dimples are observed in the low triaxiality domain, suggesting internal void shearing as the main rupture mechanism (Barsoum and Faleskog, 2007).

The volume fraction and size distribution of constituent particles influence the ductility of aluminium alloys (Pedersen et al., 2015; Thomesen et al., 2020). These particles are relatively large, typical in the range of $1 - 10$ μm, and act as nucleation sites for voids because defects are more likely to be found in large particles, thus making them less resilient to cracking (Hahn and Rosenfield, 1975; Hannard et al., 2016). The dispersoids, which are introduced to control recrystallization and grain growth, are typically approximately 0.1 μm or even smaller in size (Hannard et al., 2016). While the importance of constituent particles on ductile fracture is well established, the role of the dispersoids is less certain. It is common to accept that these particles only enter in the last stages of the fracture process when linking of voids from the larger constituent particles gives rise to microscopic stress concentrations and subsequent strain localization, which encourage nucleation of voids from these smaller particles (Hahn and Rosenfield, 1975). Coalescence may immediately follow as the conditions for void growth are already met. The contribution from the dispersoids can be recognized as smaller and more densely packed dimples on the fracture surface. Broek (1973) observed for a wide variety of different aluminium alloys that the spacing between intermediate inclusions correlates to the average dimple size on the fractured surface, which supports the role of the dispersoids. Moreover, the presence of a second population of smaller voids has been found to accelerate damage and lead to a reduction in ductility (Cox and Low, 1974; Faleskog and Shih, 1997; Tvergaard, 1998). The fine hardening precipitates, another class of particles typical in the range of a few nanometres in size, are assumed only to contribute to the fracture process by altering the strength and strain hardening of the matrix material (Hahn and Rosenfield, 1975).

Analytical and numerical methods to describe the microscopic mechanisms of ductile fracture have been researched for decades. Porous plasticity models include these mechanisms by considering a micro-mechanically motivated homogenized material based on the Hill-Mandel homogenization theory (Mandel, 1966; Hill, 1967). The underlying microscopic physical mechanisms, such as void nucleation, growth and coalescence, are accounted for through the evolution of some appropriate microstructural variable at the homogenized material level. The Gurson model (Gurson, 1977) is the most widely recognized porous plasticity model. Tvergaard (1981, 1982) later modified the Gurson model to achieve better agreement with unit cell calculations by introducing three fitting parameters in the yield function. Extensions of the Gurson model that account for nucleation (Chu and Needleman, 1980), coalescence (Tvergaard and Needleman, 1984) and shearing (Nahshon and Hutchinson, 2008) of voids have also been proposed in the literature.

In its original form, the Gurson model only considers the volume fraction of voids (or the porosity), whereas the effects of the size of the voids are not accounted for. As the void-size becomes smaller than some intrinsic material length, the Gurson model becomes questionable. As stated by Hutchinson (2000): "*Application of void growth prediction based on the conventional plasticity to submicron-sized voids is probably unjustified*". The plasticity of a hardening metallic material is governed by the total density of statistically stored and geometrically necessary dislocations. While statistically stored dislocations (SSDs) are created in homogeneous plastic straining, the density of geometrically necessary dislocations (GNDs) scales with the gradient of the plastic strain field. At the microscale, strongly size-dependent plasticity can be observed because microstructural constraints, such as small particles, introduce a considerable increase in GNDs (Ashby, 1970; Poole et al., 1996; Gao et al., 1999). Size-dependent plastic behaviour has been confirmed experimentally by micro-twist (Fleck et al., 1994), micro-indentation (Stelmashenko et al., 1993; Ma and Clarke, 1995; Nix and Gao, 1998) and micro-bending (Stölken and Evans, 1998) tests. In a numerical study, Fleck and Hutchinson (1997) considered the size effect on void growth for an isolated spherical void embedded in a strain gradient enhanced solid. In general, small voids are less prone to grow compared to larger voids, as they tend to generate a large gradient in the strain field. Similar findings were later reported by Huang et al. (2000) and Li and Huang (2005).

Modified Gurson-type yield functions that account for size effects have been proposed in the literature, starting with the model of Li et al. (2003) and Wen et al. (2005). Recently, Niordson and Tvergaard (2019) heuristically enriched the Gurson-Tvergaard model to account for size-effects. Based on results from unit cell simulations of a void embedded in a strain gradient enhanced material, they proposed to introduce size-effects into the yield surface by lowering the effective void volume fraction and reducing the hydrostatic stress sensitivity. Monchiet and Bonnet (2013) used limit analysis on a hollow sphere made of a strain gradient enhanced solid to show that the yield surface of the Gurson model could be enriched to capture void size effects by making the influence of the hydrostatic stress on yielding void size dependent. It was shown that voids with a size in the same range as the intrinsic material length grow slower than larger voids. Moreover, smaller voids result in a higher material yield stress, particularly at large stress triaxialities. For very large voids compared to the intrinsic material length, the Monchiet-Bonnet model conveniently coincides with the Gurson model.

Micromechanical unit cell calculations for ductile materials that contain primary and secondary voids of different length scales have been performed for tension (Fabrègue and Pardoen, 2008) and intense shearing (Nielsen and Tvergaard, 2011). Both studies consider an explicitly modelled void embedded in a matrix material described by the Gurson-Tvergaard model, but extended to include nucleation (Chu and Needleman, 1980). Using such a representation of the matrix material yields an upper bound for the influence of a secondary population of voids and can only be justified when these voids are large compared to the intrinsic material length. The

ductility was found to decrease with the presence of secondary voids that nucleated and grew in-between the larger primary voids. Fabrègue and Pardoen (2008) showed that the presence of a secondary population of voids does not substantially affect the growth of the first population but results in an acceleration of the coalescence phase. Similar behaviour was reported by Tvergaard (1998) when the secondary voids were explicitly introduced in the finite element mesh. Moreover, primary voids that have an oblate shape promote the nucleation and growth of secondary voids (Fabrègue and Pardoen, 2008).

This numerical study aims to disclose the possible effects of the dispersoids on the ductile fracture process in a structural aluminium alloy using finite-element based unit cell simulations. The unit cell consists of a spherical primary void embedded in a matrix material, which, to account for the secondary voids, is described by the Monchiet-Bonnet porous plasticity model with void size effects. The single, primary void of the unit cell is assumed nucleated on a constituent particle, whereas the secondary, smaller voids in the matrix are assumed nucleated on dispersoids. Proportional loading of the unit cell using multipoint constraints ensures a constant macroscopic stress triaxiality and Lode parameter during deformation. The paper is structured as follows. Section 2 presents the material parameters used in the numerical study, which are representative for a 6000-series aluminium alloy in the cast and homogenized condition. The Monchiet-Bonnet porous plasticity model, which defines the matrix material behaviour, is described in Section 3, whereas Section 4 presents the setup for the finite-element based unit cell calculations. The results from the unit cell calculations are presented and discussed in Section 5, while some concluding remarks are given in Section 6.

2. Material parameters

The study of Thomesen et al. (2020) on the plastic flow and fracture of cast and homogenized 6000-series aluminium alloys makes the basis for the material parameters used in the numerical study. The selected alloy is the AA6110 alloy in the T6 temper, which is an alloy with a 0.2% proof stress of 310 MPa.

Thomesen et al. (2020) performed uniaxial tension tests on smooth axisymmetric specimens aligned so that the tensile axis of the specimen coincided with the longitudinal axis of the billet. After machining, the specimens were solution heat-treated and artificially aged to T6 temper. Three repeat tests were conducted in a universal testing machine with a crosshead velocity of 1 mm/min. The force was measured directly from the load cell, while a contactless laser gauge was used to continuously record the smallest diameter of the cross-section of the specimen. The flow stress curve to fracture was determined from the tests using the Bridgman-LeRoy correction to obtain the flow stress in the post-necking region. A three-term Voce hardening rule was used by Thomesen et al. (2020) to represent the work-hardening of the material. The flow stress σ_{M} reads

$$\sigma_{\mathrm{M}} = \sigma_0 + \sum_{i=1}^{3} Q_i \left(1 - e^{-C_i p}\right) \tag{1}$$

where σ_0 is the initial yield stress, p is the equivalent plastic strain, and Q_i and C_i are the hardening parameters. The material parameters governing the elastic and plastic behaviour of the material are compiled in Table 1, where the elastic constants are given typical values for aluminium alloys from the literature.

The size distribution of the constituent particles for the AA6110 alloy was found by image processing on backscattered electron micrographs. A total of 30 images were taken over the surface to determine the particle size distribution. The largest equivalent diameter of the constituent particles was found to be approximately 4 μm, where the equivalent diameter reads $d_{\mathrm{p}} = \sqrt{4A_{\mathrm{p}}/\pi}$, and the area of the constituent particle in the image plane is denoted A_{p}. The total area fraction of constituent particles was calculated to be 0.0076. In accordance with the Delesse principle (Underwood, 1970), the initial volume fraction of constituent particles $f_{\mathrm{p},0}$ is approximated to be 0.0076. We have in this work used a volume fraction of 0.007 for the primary voids.

An estimate of the size and distribution of the dispersoids was obtained from simulations using the microstructure-based model Alstruc (Dons, 2001), which depends on standard solidification and diffusion theory. From the chemical composition of the alloy, the grain size and the secondary dendrite arm spacing, one can find estimates on the type, volume fraction and size of different particles. The equivalent diameter of the dispersoids $d_{\mathrm{s},0}$ was estimated to be approximately 0.1 μm, while the initial volume fraction $f_{\mathrm{s},0}$ was set to 0.005. According to Evans and Hutchinson (2009), there seems to be a strong inverse correlation between the intrinsic material length l_1 introduced in the Fleck-Hutchinson theory (Fleck and Hutchinson, 1997) and the yield strain in a wide range of metallic alloys. Based on Fig. 13 in their paper, it is reasonable to assume an intrinsic material length of the AA6110 alloy in temper T6 to be within the interval 0.01 μm $< l_1 <$ 0.1 μm. For the purpose of this study, it is enough to consider the range 0.01 μm $\leq l_1 \leq$ 0.05 μm. All material parameters are compiled in Table 1.

Table 1
Material data for the AA6110-T6 aluminium alloy (Thomesen, 2019).

Elastic constants		Yield stress and isotropic strain hardening						
E[MPa]	ν[-]	σ_0[MPa]	Q_1[MPa]	C_1[-]	Q_2[MPa]	C_2[-]	Q_3[MPa]	C_3[-]
70000	0.3	277.7	35.9	1311.7	63.6	19.1	6888.4	0.01

Tvergaard parameters			Constituent particles		Dispersoids		Intrinsic length	
q_1[-]	q_2[-]	q_3[-]	$f_{\mathrm{p},0}$[-]	$d_{\mathrm{p},0}$[μm]	$f_{\mathrm{s},0}$[-]	$d_{\mathrm{s},0}$[μm]	l_1[μm]	
1.5	1.0	2.25	0.007	4.0	0.005	0.1	0.01 − 0.05	

The reader is referred to Thomesen (2019) and Thomesen et al. (2020) for the chemical composition, homogenization, artificial ageing, material characterization and mechanical testing of the AA6110 alloy used herein.

3. Constitutive model of the matrix material

Monchiet and Bonnet (2013) developed a Gurson-type macroscopic yield criterion that accounts for void size effects. Following the approach of Gurson (1977), an upper-bound limit load analysis on a rigid-perfect plastic hollow sphere embedded in a matrix material that obeys the strain gradient plasticity model of Fleck and Hutchinson (1997) was used to obtain the macroscopic yield criterion for a porous plastic material with void size effects. A hypoelastic-plastic formulation of the Monchiet-Bonnet model is applied here to allow for large deformations. The corotational stress approach is used to account for large rotations (Belytschko et al., 2014), and henceforward $\widehat{(\circ)}$ denotes a corotated tensor, i.e., a tensor $(\circ)$ expressed in a local material system that follows the local spin of the material point.

Assuming small elastic deformations, the corotated rate-of-deformation tensor $\widehat{\mathbf{D}}$ is additively split into an elastic and a plastic part, viz.

$$\widehat{\mathbf{D}} = \widehat{\mathbf{D}}^{e} + \widehat{\mathbf{D}}^{p} \tag{2}$$

The corotated stress tensor $\widehat{\boldsymbol{\sigma}}$ and the corotated rate-of-deformation tensor $\widehat{\mathbf{D}}$ are defined by

$$\widehat{\boldsymbol{\sigma}} = \mathbf{R}^{T} \cdot \boldsymbol{\sigma} \cdot \mathbf{R} \tag{3}$$

$$\widehat{\mathbf{D}} = \mathbf{R}^{T} \cdot \mathbf{D} \cdot \mathbf{R} \tag{4}$$

where $\boldsymbol{\sigma}$ is the Cauchy stress tensor and $\mathbf{D}$ is the rate-of-deformation tensor expressed in the fixed global coordinate system. The transformation from the local material system to this fixed global system is defined by the orthogonal rotation tensor $\mathbf{R}$.

Under the assumption of linear isotropic elasticity, the hypoelastic formulation relates the corotated stress rate tensor $\dot{\widehat{\boldsymbol{\sigma}}}$ and the elastic rate-of-deformation tensor $\widehat{\mathbf{D}}^{e}$ according to the generalized Hooke's law

$$\dot{\widehat{\boldsymbol{\sigma}}} = \frac{E}{1+\nu}\widehat{\mathbf{D}}^{'e} + \frac{E}{3(1-2\nu)}\mathrm{tr}\left(\widehat{\mathbf{D}}^{e}\right)\mathbf{I} \tag{5}$$

where E is the elastic modulus and ν is the Poisson's ratio. The deviatoric and volumetric parts of the elastic rate-of-deformation tensor are denoted $\widehat{\mathbf{D}}^{'e}$ and $\frac{1}{3}\mathrm{tr}(\widehat{\mathbf{D}}^{e})\mathbf{I}$, respectively, where $\widehat{\mathbf{D}}^{'e} = \widehat{\mathbf{D}}^{e} - \frac{1}{3}\mathrm{tr}(\widehat{\mathbf{D}}^{e})\mathbf{I}$ and $\mathbf{I}$ is the second-order identity tensor.

The macroscopic yield criterion of the Monchiet-Bonnet model is defined by (Monchiet and Bonnet, 2013)

$$\Phi(\widehat{\boldsymbol{\sigma}}, f, \sigma_{\mathrm{M}}, \eta) = \left(\frac{\sigma_{\mathrm{eq}}}{\sigma_{\mathrm{M}}}\right)^{2} + 2q_{1}f\cosh\left(\frac{3}{2\eta}q_{2}\frac{\sigma_{\mathrm{H}}}{\sigma_{\mathrm{M}}}\right) - \left(1 + q_{3}f^{2}\right) \leq 0 \tag{6}$$

where $\Phi = 0$ defines the periphery and $\Phi < 0$ the interior of the elastic domain. The von Mises equivalent stress and the hydrostatic stress are expressed as $\sigma_{\mathrm{eq}} = \sqrt{\frac{3}{2}\widehat{\boldsymbol{\sigma}}^{'} : \widehat{\boldsymbol{\sigma}}^{'}}$ and $\sigma_{\mathrm{H}} = \frac{1}{3}\mathrm{tr}(\widehat{\boldsymbol{\sigma}})$, respectively, where $\widehat{\boldsymbol{\sigma}}^{'} = \widehat{\boldsymbol{\sigma}} - \sigma_{\mathrm{H}}\mathbf{I}$ is the deviatoric stress tensor, here expressed in the corotated coordinate system. It is emphasized that the stress tensor is normally interpreted as a macroscopic quantity in porous plasticity. We will use lowercase letters here to avoid any confusion with the macroscopic stresses applied to the unit cell boundaries in Section 4, which are denoted by capital letters. The porosity f, the flow stress of the matrix material σ_{M} and the variable η are considered internal microscopic quantities. The parameters q_1, q_2 and q_3 introduced by Tvergaard (1981, 1982) were not incorporated in the original formulation by Monchiet and Bonnet (2013). If the porosity f equals to zero, Eq. (6) takes the form of the von Mises yield criterion. Moreover, the yield function is fulfilled for zero stresses (i.e. $\sigma_{\mathrm{eq}} = \sigma_{\mathrm{H}} = 0$) at a certain porosity level, defined by $f = q_1^{-1}$ for $q_3 = q_1^2$, which implies that the yield function collapses into a single point and the material loses its load-carrying capacity. Thus, for $q_3 = q_1^2$ the porosity must be $f < q_1^{-1}$. The initial porosity is denoted f_0.

The work hardening of the matrix material is heuristically introduced into σ_{M} using the three-term Voce hardening rule in Eq. (1). By assuming a plastically incompressible matrix material, the evolution of the porosity f can be expressed according to

$$\dot{f} = (1-f)\mathrm{tr}\left(\widehat{\mathbf{D}}^{p}\right) \tag{7}$$

Only the contribution of void growth is considered in this work, and any contributions from nucleation (Chu and Needleman, 1980) and the effects of the deviatoric stress state (Nahshon and Hutchinson, 2008) have been excluded.

The corotated plastic rate-of-deformation tensor $\widehat{\mathbf{D}}^{p}$ can be determined from the associated flow rule as the homogenization process preserves normality (Gurson, 1977). Thus

$$\widehat{\mathbf{D}}^{p} = \dot{\lambda}\frac{\partial\Phi}{\partial\widehat{\boldsymbol{\sigma}}} = \dot{\lambda}\left[\frac{3}{\sigma_{\mathrm{M}}^{2}}\widehat{\boldsymbol{\sigma}}^{'} + \frac{fq_{1}q_{2}}{\eta\sigma_{\mathrm{M}}}\sinh\left(\frac{3}{2\eta}q_{2}\frac{\sigma_{\mathrm{H}}}{\sigma_{\mathrm{M}}}\right)\mathbf{I}\right] \tag{8}$$

where $\dot{\lambda}$ is the plastic multiplier. The first term in Eq. (8) gives the deviatoric part, while the second term defines the volumetric part of the plastic rate-of-deformation tensor. From Eq. (7) it is clear that only the volumetric part contributes to void growth and thus only spherical void growth is allowed for. The equivalent microscopic plastic strain rate $\dot{p}$ is given from the equivalence in plastic power, defined as

$$\hat{\boldsymbol{\sigma}} : \hat{\mathbf{D}}^{\mathrm{p}} = (1-f)\sigma_{\mathrm{M}}\dot{p} \tag{9}$$

The Monchiet-Bonnet model clearly has the same properties as the classical Gurson-Tvergaard model. However, the additional non-dimensional variable η induces a void size dependency by modifying the hydrostatic stress sensitivity of the yield function Φ. The variable η enters as an approximation in the integration of the volume average macroscopic potential. Owing to the introduction of strain rate gradient terms in the modified equivalent strain rate, this approximation is necessary to find a closed-form solution of the macroscopic yield criterion. This approximation agrees well with numerical integration of the macroscopic potential (Monchiet and Bonnet, 2013). The non-dimensional variable η is calculated as

$$\eta = \frac{3}{\ln(f)}\left[\operatorname{arcsinh}\left(\frac{\alpha}{u}\right) - \sqrt{1 + \left(\frac{u}{\alpha}\right)^2}\,\right]_{u=f^{1/3}}^{u=1} \tag{10}$$

with

$$\alpha = \frac{1}{3}\sqrt{\frac{2}{5}}\frac{a}{l_1} \tag{11}$$

Here, a is the radius of the spherical void and l_1 is an intrinsic material length introduced by the strain gradient plasticity model of Fleck and Hutchinson (1997). Experimental findings suggest that the intrinsic material length is in the micrometre range (Fleck et al., 1994; Stölken and Evans, 1998). Owing to the matrix incompressibility, it is possible to relate the growth in void size to the growth of the porosity (Monchiet and Bonnet, 2013). Accordingly, the evolution for the internal material variable α is obtained as

$$\dot{\alpha} = \frac{\alpha}{3f(1-f)}\dot{f} = \frac{\alpha}{3f}\operatorname{tr}\left(\hat{\mathbf{D}}^{\mathrm{p}}\right) \tag{12}$$

The evolution of η is obtained from the time derivative of Eq. (10). By substituting for $\dot{f}$ and $\dot{\alpha}$ with the rate equations established above, we arrive at

$$\dot{\eta} = \frac{1}{f\ln(f)}\left[\sqrt{1 + \frac{1}{\alpha^2}} - f\sqrt{1 + \frac{f^{2/3}}{\alpha^2}} - (1-f)\eta\right]\operatorname{tr}\left(\hat{\mathbf{D}}^{\mathrm{p}}\right) \tag{13}$$

Eqs. (7), (9) and (13) complete the evolution rules for the three internal quantities which appear in the yield function Φ.

The ratio between the initial void radius a_0 and the intrinsic material length l_1 is the only additional material parameter in the Monchiet-Bonnet model compared to the Gurson model. The evolution of void radius a follows from Eqs. (11) and (12). Fig. 1 (a) shows the yield surface in the normalized equivalent-hydrostatic stress space for various ratios a/l_1. It appears that the yield surface domain gradually increases for decreasing values of a/l_1, which is of particular importance for high hydrostatic stress states. The void size does
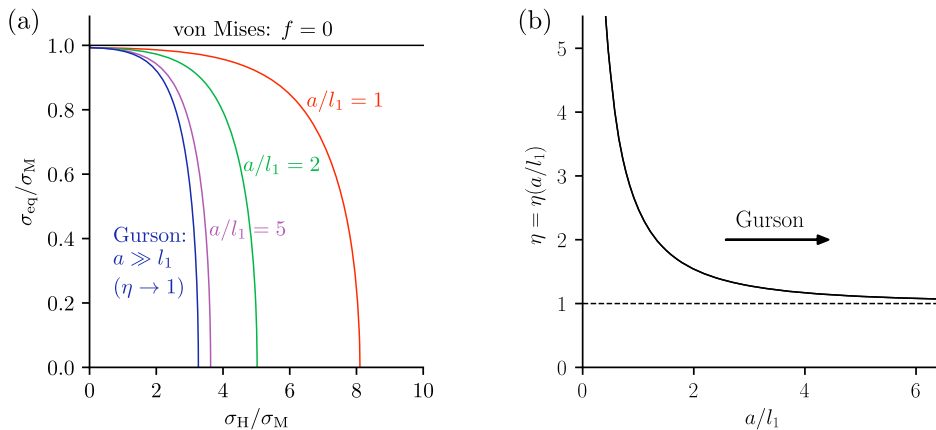

Fig. 1. (a) The von Mises yield locus (black line) and the yield loci of the Monchiet-Bonnet model (coloured lines) for various ratios a/l_1 in the normalized equivalent-hydrostatic stress space. The blue curve shows the yield locus of the Gurson-Tvergaard model. (b) The evolution of the non-dimensional variable η in Eq. (10) with a/l_1. The original Tvergaard parameters ($q_1 = 1.5$, $q_2 = 1.0$, $q_3 = 2.25$) and a matrix porosity $f = 0.005$ have been used in the illustrations.

not influence the yield surface in purely deviatoric load cases ($\sigma_H = 0$). The non-dimensional variable η in Eq. (10) is plotted in Fig. 1 (b) as a function of a/l_1. For large voids, i.e., when a is large compared to l_1, η tends towards unity and Eq. (6) conveniently takes the form of the Gurson-Tvergaard model. In contrast, if $a \ll l_1$, η becomes large and prevents void growth because the volumetric part of the plastic rate-of-deformation tensor $\widehat{\mathbf{D}}^p$ vanishes. This results in a pressure-insensitive yield criterion similar to the von Mises yield criterion. The reduction in the rate of void growth can be explained by the presence of a strong strain gradient, which increases the hardening of the material in the vicinity of the void cavity.

The constitutive relations are completed by the Kuhn-Tucker conditions

$$\Phi \leq 0, \ \dot{\lambda} \geq 0, \ \Phi\dot{\lambda} = 0 \tag{14}$$

which distinguish between elastic loading/unloading and plastic loading. A stress-update algorithm is used to ensure that these constraints are fulfilled, and here the temporal integration of the constitutive equations is carried out using the cutting plane algorithm (Ortiz and Simo, 1986). The consistent tangent modulus is evaluated numerically. A user-defined material subroutine (UMAT) is used to implement the Monchiet-Bonnet model in ABAQUS/Standard 6.14. To ensure sufficient stability and accuracy of the stress-update algorithm, a sub-stepping scheme is employed whenever the norm of the deviatoric strain increment $\Delta\bar{\varepsilon}$ exceeds a threshold given by

$$\Delta\bar{\varepsilon} = \Delta t \sqrt{\widehat{\mathbf{D}}' : \widehat{\mathbf{D}}'} > 0.01 \frac{\sigma_0}{E} \tag{15}$$

where Δt is the current time increment. The deviatoric strain increment $\Delta\widehat{\varepsilon}' = \Delta t \widehat{\mathbf{D}}'$ supplied by the finite element solver is then divided into N_S sub-steps so that the new sub-increments fulfil the above requirement, i.e., $N_S = \mathrm{nint}\left(\frac{\Delta t \sqrt{\widehat{\mathbf{D}}' : \widehat{\mathbf{D}}'}}{0.01\sigma_0/E}\right)$, where $\mathrm{nint}(\circ)$ returns the integer of the real number $(\circ)$.

4. Unit cell modelling

4.1. Stress state parameters

Important stress state parameters used in this work will be outlined in the following. All macroscopic quantities are expressed with capital letters, while lowercase letters are reserved for local microscopic quantities related to the material response of the matrix. The arbitrary stress state P in Fig. 2 (a) can be expressed as

$$\Sigma_1 = \Sigma_1' + \Sigma_H = \Sigma_{eq}\left(\frac{2}{3}\cos(\theta_L) + T\right)$$

$$\Sigma_2 = \Sigma_2' + \Sigma_H = \Sigma_{eq}\left(\frac{2}{3}\cos\left(\theta_L - \frac{2\pi}{3}\right) + T\right)$$

$$\Sigma_3 = \Sigma_3' + \Sigma_H = \Sigma_{eq}\left(\frac{2}{3}\cos\left(\theta_L + \frac{2\pi}{3}\right) + T\right) \tag{16}$$

where $\Sigma_1, \Sigma_2, \Sigma_3$ and $\Sigma_1', \Sigma_2', \Sigma_3'$ are the principal stresses and deviatoric principal stresses, respectively, $\Sigma_H = I_1/3$ is the hydrostatic stress, θ_L is the deviatoric angle and $\Sigma_{eq} = \sqrt{3J_2}$ is the von Mises equivalent stress. The first stress invariant and the second deviatoric stress
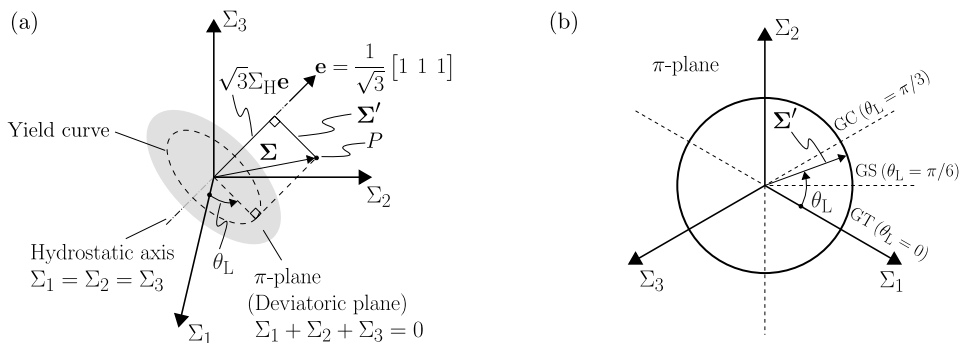

Fig. 2. Illustration of a stress point P in (a) the principal stress space and (b) the π-plane. The stress tensor is split into a hydrostatic part ($\Sigma_H\mathbf{I}$) and a deviatoric part ($\mathbf{\Sigma}'$), where $\mathbf{e}$ gives the direction of the hydrostatic axis. The yield locus takes the form of a circle in the π-plane for a von Mises material. The deviatoric angle θ_L is defined in both sub-figures. GT, GS and GC refer to generalized tension, generalized shear and generalized compression, respectively.

invariant are defined by $I_1 = \text{tr}(\boldsymbol{\Sigma})$ and $J_2 = \frac{1}{2}\boldsymbol{\Sigma}' : \boldsymbol{\Sigma}'$, respectively, where $\boldsymbol{\Sigma}$ and $\boldsymbol{\Sigma}'$ are the macroscopic stress and deviatoric stress tensors.

In Eq. (16), the stress triaxiality T has been introduced as the ratio between the hydrostatic and the equivalent stress, i.e.,

$$T = \frac{\Sigma_{\text{H}}}{\Sigma_{\text{eq}}} \tag{17}$$

which serves as an important quantity for void growth (McClintock, 1968; Rice and Tracey, 1969) and will be used to control the imposed stress state of the unit cell. The deviatoric angle θ_{L} defines the angle between the first principal axis in the π-plane and the deviatoric stress vector $\boldsymbol{\Sigma}'$, see Fig. 2 (b). As we assume an isotropic material, θ_{L} is confined to lie within the range $[0, \pi/3]$. The principal stresses are then arranged so that $\Sigma_1 \geq \Sigma_2 \geq \Sigma_3$. The Lode parameter L is related to the deviatoric angle θ_{L} by the relation

$$L = \sqrt{3}\tan\left(\theta_{\text{L}} - \frac{\pi}{6}\right) = \frac{2\Sigma_2 - \Sigma_1 - \Sigma_3}{\Sigma_1 - \Sigma_3} \tag{18}$$

It follows that $L = -1$ and $L = 1$ define the peripheral deviatoric states $\theta_{\text{L}} = 0$ (generalized tension) and $\theta_{\text{L}} = \pi/3$ (generalized compression), respectively, whereas $L = 0$ defines the deviatoric state $\theta_{\text{L}} = \pi/6$ (generalized shear).

It is clear from Eqs. (16) and (18) that the ratios between the different principal stress components $\Sigma_1, \Sigma_2, \Sigma_3$ only depend on the stress triaxiality and the Lode parameter. Evidently, any proportional stress state can be uniquely defined by these two stress invariants, while the von Mises equivalent stress controls the magnitude of the stress state.

4.2. Unit cell and finite element discretization

Fig. 3 illustrates how a realistic heterogeneous microstructure of a polycrystalline material, consisting of grains and particles of various sizes and shapes, can be reduced to a unit cell. Scanning electron microscope (SEM) images of the current aluminium alloy reveal a concentration of constituent particles at the grain boundaries, while the dispersoids are more spatially distributed in the matrix material (Thomesen et al., 2020). A highly simplified microstructure is given in Fig. 3 (b), where grains are approximated by a homogenized matrix description. The constituent particles and the dispersoids are assumed to be evenly distributed and initially of spherical shape, where the size within each population is uniform. It is emphasized that the variation in the shape and the spatial distribution of particles has been neglected, even if these parameters can have a pronounced influence on the ductile fracture process (Pardoen and Hutchinson, 2000;
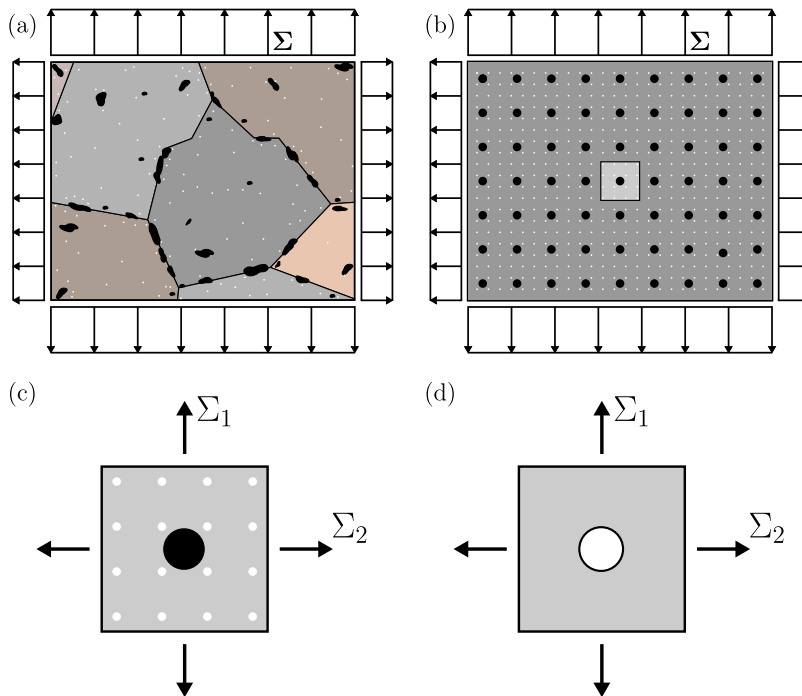

Fig. 3. The various levels of approximation from a polycrystalline solid to a unit cell. An illustration of a realistic microstructure is shown in (a), which consists of grains and particles of various shapes and sizes. The large black specks mainly located at the grain boundaries represent the constituent particles, while the small white dots more evenly distributed represent the dispersoids. A simplified microstructure, in which the grains are represented by a homogenous matrix material and both populations of particles are assumed to be evenly distributed and of equal spherical shape, is shown in (b). The resulting unit cell is presented in (c). In (d), the dispersoids have been homogenized into the matrix material as secondary voids, and the constituent particle is considered as an initial void.

Fabrègue and Pardoen, 2008). The unit cell in Fig. 3 (c) can be assembled from the homogenized microstructure.

Owing to the substantial size difference, the dispersoids cannot be discretely represented in the finite element mesh within reasonable computational effort. The effects of dispersoids are therefore incorporated in the matrix material model as described in the previous section and illustrated in Fig. 3 (d). This simplification is justified when the size of the secondary voids is much smaller than the primary voids. There is then a strict separation between the different scales, which allows for the consideration of secondary voids at the homogenized material level. The size of the primary voids must also be considerably larger than the intrinsic material length. Otherwise, the hardening arising in the matrix due to strain gradients must be considered. All voids are assumed to be pre-existing as only the growth phase will be considered in this work. This assumption might be justified for the larger particles, where particle cracking occurs more readily, but is not obvious for the small dispersoids as large stresses are often necessary to promote decohesion at the matrix-particle interface (Fabrègue and Pardoen, 2008).

Under the assumption of a uniform and periodic distribution of voids from constituent particles, finite element simulation will be used to evaluate the microscopic and macroscopic response of the cell shown in Fig. 4 (a). Shear effects have been precluded in the analyses and only normal macroscopic stress components act on the boundaries of the cell. The primary void surface is free from any tractions. Only $1/8$ of the unit cell is modelled as symmetry is exploited to reduce the computational cost. The external edges of the unit cell are assumed to be of equal length $2\bar{l}_0$, where $\bar{l}_0$ is the initial length of the $1/8$-model. The primary void is assumed initially spherical with a radius of $\bar{R}_{p,0}$. The initial void volume fraction of primary voids is then given by

$$f_{p,0} = \frac{V_{p,0}}{V_{RVE,0}} = \frac{\pi}{6}\left(\frac{\bar{R}_{p,0}}{\bar{l}_0}\right)^3 \tag{19}$$

where $V_{p,0}$ is the initial volume of the primary void and $V_{RVE,0}$ is the total volume of the unit cell in the undeformed configuration. As the initial volume fraction $f_{p,0}$ and void radius $\bar{R}_{p,0}$ of constituent particles are known for this AA6110 alloy (see Table 1), the initial length $\bar{l}_0$ of the unit cell can be determined. Periodic boundary conditions are enforced by restricting the external boundaries to remain straight throughout the deformation. The prescribed displacement of the nodes located on the rigid walls is controlled through non-linear kinematical constraints so that the stress triaxiality ratio T (Eq. (17)) and the Lode parameter L (Eq. (18)) are maintained constant. A multi-point constraints (MPC) user subroutine is used to ensure that that the macroscopic deformation power of the cell equals to its volume-average counterpart in accordance with Hill-Mandel homogenization theory (Mandel, 1966; Hill, 1967). The method is detailed in Dæhli et al. (2017) and will not be further explained in this study.

The implicit FE software ABAQUS/Standard 6.14 is utilized to perform the finite element simulations. A study on mesh convergence showed that a cell configuration consisting of 2080 linear hexagonal elements with selective reduced integration (C3D8 in ABAQUS) adequately described the cell response. The spatially discretized FE-model is shown in Fig. 4 (b). Details of this study have been omitted herein for brevity.

4.3. Calculation of stress, strain and porosities of the unit cell

The macroscopic stress tensor $\boldsymbol{\Sigma}$ applied to the cell is calculated as a volume average of the stresses in all integration points

$$\boldsymbol{\Sigma} = \frac{1}{V_{mat}}\sum_{j=1}^{n_{int}}\boldsymbol{\sigma}_j V_j, \quad V_{mat} = \sum_{j=1}^{n_{int}} V_j \tag{20}$$
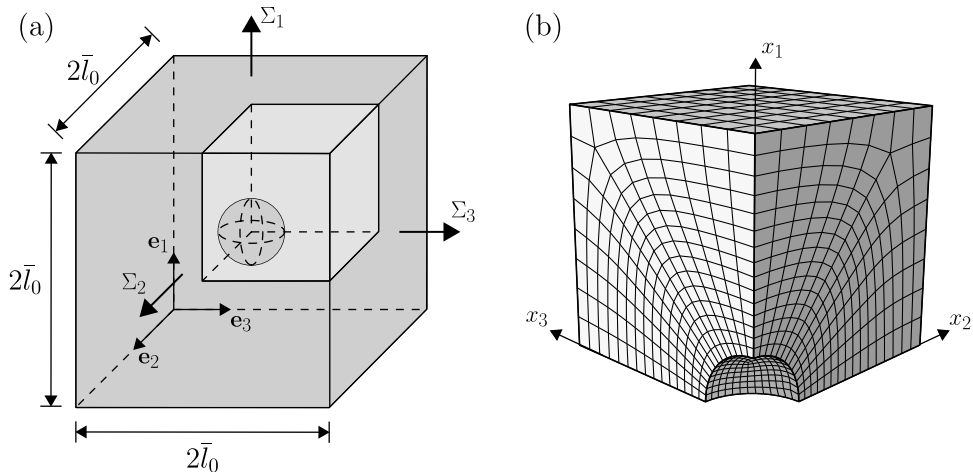

Fig. 4. (a) Illustrates the unit cell, where the $1/8$-model is indicated with a light grey colour, while (b) gives the spatially discretized FE-model of the $1/8$-model (Dæhli et al., 2017).

where σ_j and V_j are the Cauchy stress and current volume associated with integration point j, respectively, V_{mat} is the total material volume associated with the matrix and n_{int} is the total number of integration points. The porosity of the primary void f_{p} is calculated from

$$f_{\text{p}} = \frac{V_{\text{P}}}{V_{\text{RVE}}}, \quad V_{\text{RVE}} = \bar{l}_1\bar{l}_2\bar{l}_3 \tag{21}$$

where $\bar{l}_1, \bar{l}_2, \bar{l}_3$ are the side length of the 1/8-model in the current configuration and $V_{\text{p}} = V_{\text{RVE}} - V_{\text{mat}}$ is the volume of the cavity associated with the discretely represented primary void. The porosity of secondary voids f_{s} in the matrix material is evaluated as the volume average in the same manner as the macroscopic stress, i.e.,

$$f_{\text{s}} = \frac{V_{\text{s}}}{V_{\text{mat}}}, \quad V_{\text{s}} = \sum_{j=1}^{n_{\text{int}}} f_j V_j \tag{22}$$

where f_j is the porosity in integration point j and V_{s} is the total volume of secondary voids. It is emphasized that f is the local porosity of secondary voids associated with the Monchiet-Bonnet model in Section 3, and should henceforward not be confused with the volume average counterpart f_{s}. The total porosity is calculated from

$$f_{\text{tot}} = \frac{V_{\text{p}} + V_{\text{s}}}{V_{\text{RVE}}} \tag{23}$$

where $V_{\text{p}} + V_{\text{s}}$ contains the volume of all cavities inside the cell.

An equivalent macroscopic strain measure E_{eq} is used to compare the macroscopic stress response and the void volume fraction evolution. We define

$$E_{\text{eq}} = \sqrt{\frac{2}{3}\mathbf{E}' : \mathbf{E}'} \tag{24}$$

where $\mathbf{E}' = \mathbf{E} - \frac{1}{3}\text{tr}(\mathbf{E})\mathbf{I}$ is the deviatoric part of the macroscopic strain $\mathbf{E}$. The macroscopic principal logarithmic strain components are calculated from the current unit cell configuration as

$$E_1 = \ln\left(\frac{\bar{l}_1}{\bar{l}_0}\right), E_2 = \ln\left(\frac{\bar{l}_2}{\bar{l}_0}\right), E_3 = \ln\left(\frac{\bar{l}_3}{\bar{l}_0}\right) \tag{25}$$

The point of coalescence is defined as the point at which the strain state shifts to a mode of uniaxial straining in the tensile direction (Koplik and Needleman, 1988). Localization of plastic strains in the inter-void ligament, that is the x_2x_3-plane in Fig. 4, occurs subsequent to this point, while the material outside the ligament unloads elastically. Physically, this represents the link-up with a neighbouring primary void from an adjacent unit cell.

5. Numerical results

The unit cell from Section 4.2 will be deformed in a displacement-controlled manner with an imposed proportional stress state so that the stress triaxiality and the Lode parameter are constant during the simulation. We start by considering a Lode parameter equal to -1, which corresponds to a state of generalized tension associated with the stress state in the centre of axisymmetric specimens where $\Sigma_1 > \Sigma_2 = \Sigma_3$. Other deviatoric stress states are discussed at the end of this section. The stress triaxiality is varied sequentially from 0.6 to 3.0, which corresponds to the stress state occurring in a slightly notched axisymmetric tensile specimen to the stress state in front of a crack tip (Benzerga and Leblond, 2010). Lower stress triaxialities may result in void closing and can lead to questionable results in the absence of a physical particle inside the centre cavity.

By altering the matrix material in the unit cell, effects from a secondary population of voids can be included. The pressure insensitive von Mises material model, which corresponds to no secondary voids, will be solved directly with a radial return mapping algorithm (Simo and Hughes, 1998), and not as the special case $f = 0$ in Eq. (6), to avoid any complications with the undefined logarithmic term in Eq. (10) when zero porosity is defined. Moreover, a Gurson-Tvergaard material is readily obtained by assigning l_1 a low value so that η is close to unity. Any responses in between these two extremes are obtained by decreasing the intrinsic material length l_1 (or, equivalently, increasing the initial ratio a_0/l_1). This way, the contribution from a secondary population is directly controlled through l_1. Note that the ratio a/l_1 increases with the plastic deformation as the void radius a increases with the matrix porosity f. Thus, the value of a_0/l_1 only refers to the initial state, where the initial radius of the secondary voids $a_0 = \frac{1}{2}d_{\text{s},0}$ equals 0.05 μm (see Table 1). Fig. 1 (a) shows the normalized equivalent stress as a function of the normalized hydrostatic stress for the different matrix materials used in this work, assuming a matrix porosity of $f = 0.005$. As the initial radius $\bar{R}_{\text{p},0}$ and volume fraction $f_{\text{p},0}$ of the primary void are 2.0 μm and 0.007, respectively, Eq. (19) yields an initial unit cell side length $\bar{l}_0$ of 8.43 μm. We emphasize that the porosity and equivalent void radius related to the primary void are used to generate the geometry of the computational cell, while the secondary porosity, which is linked to nucleation of voids on the dispersoids, is incorporated in the porous plasticity model applied for the matrix.

5.1. Macroscopic stress-strain response

Fig. 5 (a) and (b) present the macroscopic von Mises equivalent stress and the primary porosity evolution as a function of the macroscopic equivalent strain for Lode parameter $L = -1$ and stress triaxiality of 0.8 and 2.0. The results for $L = 0$ and $L = 1$ will be discussed in Section 5.5. Higher triaxiality markedly reduces the overall stress level and the strain at coalescence for all values of the intrinsic material length l_1 due to a faster growth of the primary void. At a given stress triaxiality, there is a decrease in both the overall stress level and the strain at coalescence with decreasing values of l_1. The reason is the faster growth of the secondary voids and the associated softening of the matrix material in the inter-void ligament.

Fig. 6 displays the deformed cell configuration in the x_1x_2- and x_2x_3-planes at the end of the curves in Fig. 5 (a) and (b) for stress triaxiality equal to 0.8 (Fig. 6 (a)) and 2.0 (Fig. 6 (b)) with different internal material lengths l_1. Note that the coordinate axes in Fig. 6 coincide with the coordinate axes in Fig. 4 (b). The distribution of the secondary porosity is included as contours in the plots. The 1/8-cell model is mirrored about the x_3x_1-plane and the surface of the primary void cavity is not included in the contour plot to accentuate its shape. Using von Mises plasticity for the matrix material, the inter-void ligament necks down to almost zero width, due to the absence of the secondary population of voids. In contrast, only a minor reduction of the ligament material thickness is observable for the Gurson-Tvergaard matrix material. As seen from Fig. 6, the reduction of the overall stress level complies with the softening of the inter-void ligament material due to fast growth of the secondary voids in this region. An intrinsic material length l_1 of and 0.025 µm in the Monchiet-Bonnet model yields a macroscopic and microscopic response in-between these two extremes as the inter-void ligament material is less prone to softening when the initial ratio a_0/l_1 decreases. This ratio must be greater than 1 in order to find any significant effects from the secondary voids in the matrix material.
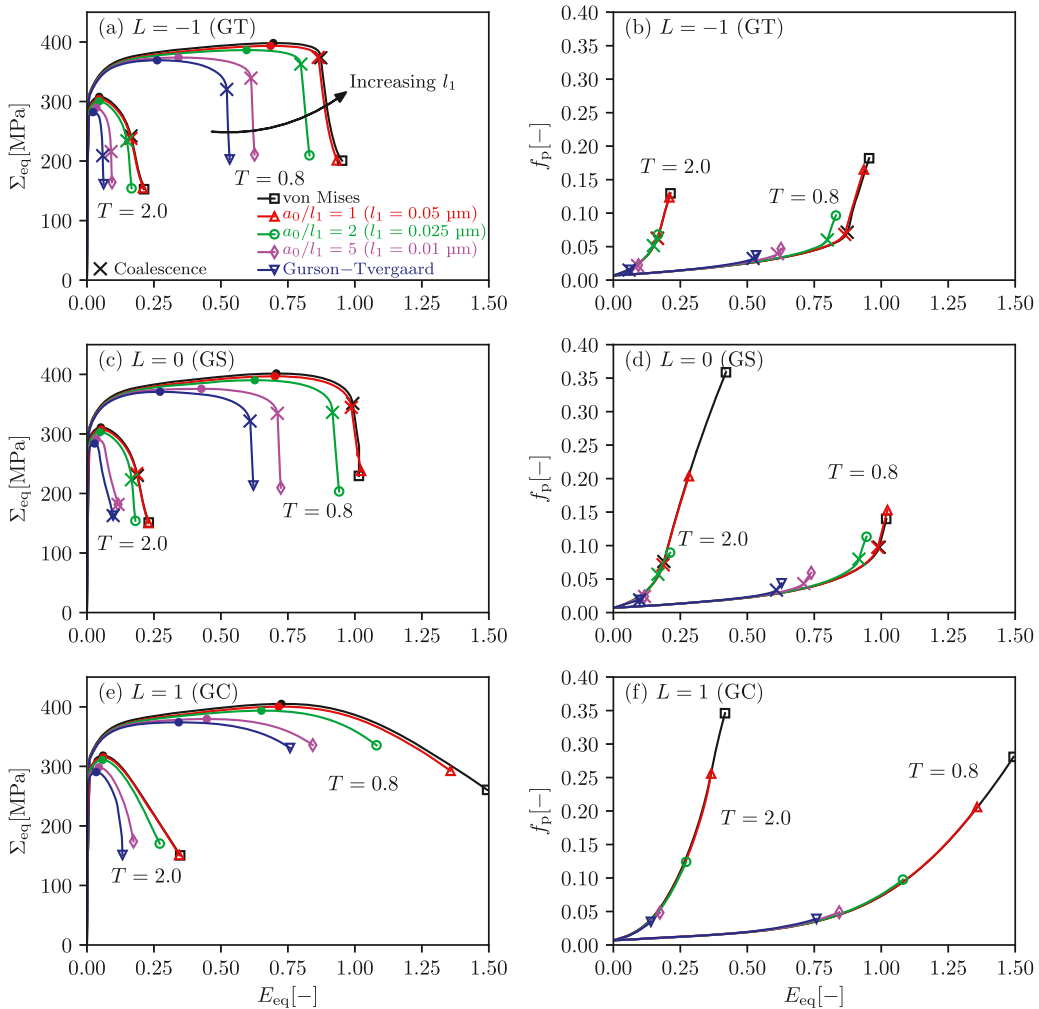

Fig. 5. (a)(c)(e) Macroscopic equivalent stress Σ_{eq}, and (b)(d)(f) porosity of the primary void f_p as a function of the macroscopic equivalent strain E_{eq} for a stress triaxiality equal to 0.8 and 2.0. The colour of the curves gives the model used in the matrix material, as described in figure (a). The point of coalescence is indicated by a cross (×) and the peak stress is indicated by a circle (•).
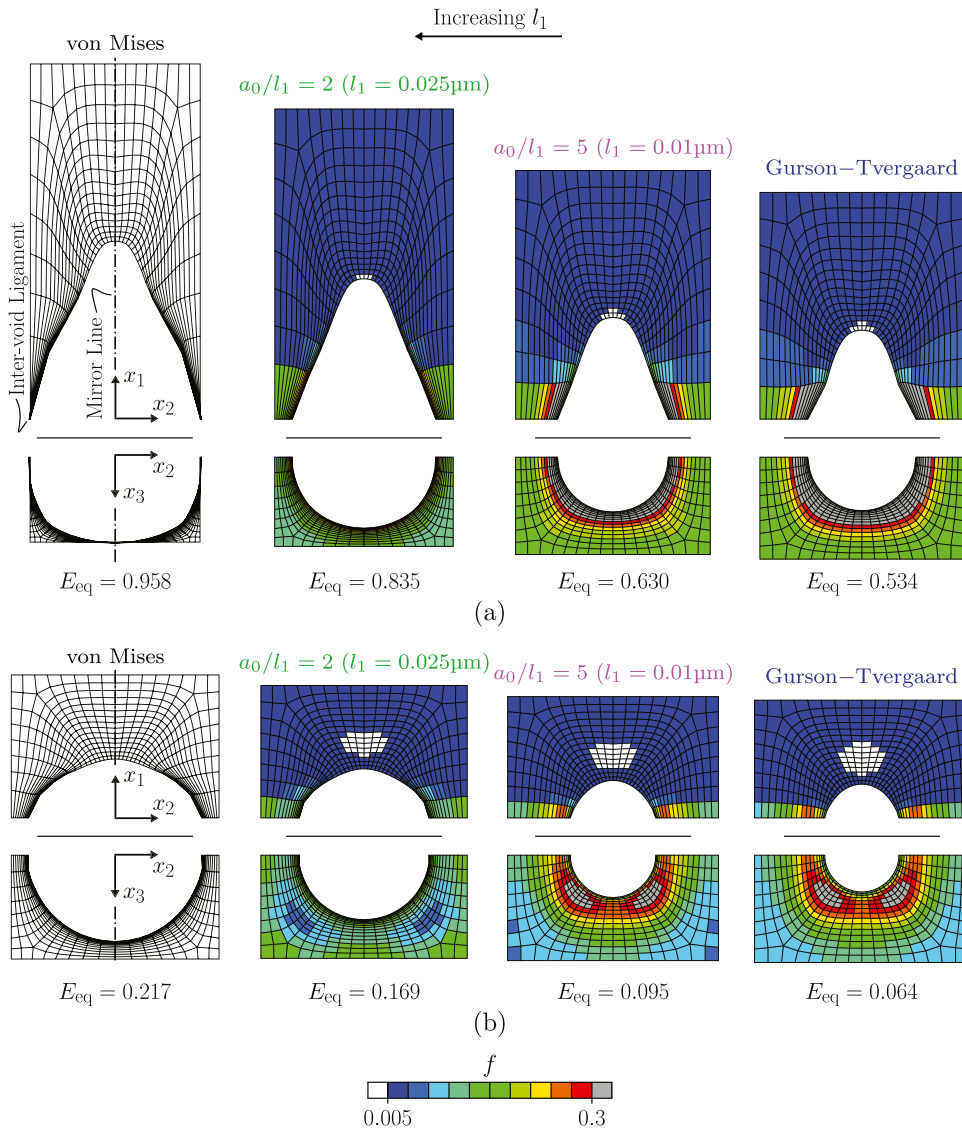
Fig. 6. The unit cell configuration at the end of the curves in Figure 5 (a) and (b) for a stress triaxiality T equal to (a) 0.8 and (b) 2.0 and $L = -1$. Only the cell walls at the $x_1 x_2$- and $x_2 x_3$-planes are included, where the coordinate axes coincides with the coordinate axes in Figure 4 (b). The 1/8-cell model is mirrored about the $x_3 x_1$-plane and the surface of the cavity is not included in the contour plot to accentuate the shape of the primary void. The contour plot shows the local porosity from secondary voids $f \in [0.005, 0.3]$. Any elements with values below or above this range are given a light or dark grey colour, respectively.

5.2. Void growth and coalescence phase

The porosity of primary voids f_{p} as a function of the macroscopic equivalent strain is shown in Fig. 5 (b) for the case of $L = -1$. Initially, the presence of secondary voids growing in the matrix material does not affect the growth of the primary voids. It does, however, accelerate the point of coalescence, which complies with findings by Fabrègue and Pardoen (2008). Though the growth of f_{p} is essentially unaffected, the overall stress level of the unit cell is still reduced as previously discussed. Fabrègue and Pardoen (2008) did not report such large reductions in macroscopic stress level prior to coalescence, possibly because they included nucleating phases and assumed no pre-existing secondary void population.

In the case of a triaxiality equal to 0.8, a sudden rise in f_{p} occurs after the onset of coalescence, indicated by a cross ($\times$) in the graphs. This rise becomes more pronounced with higher values of the intrinsic material length l_1 due to a shift in failure mechanism, as can be seen from the deformed unit cells in Fig. 6 (a). When the growth of secondary voids is slow or absent, the primary voids can grow after the onset of coalescence, and the failure mode becomes necking-down of the inter-void ligament material. With faster growth of the secondary population of voids, i.e., for lower values of l_1, the material in the inter-void ligament will soften and eventually fail before extensive growth of the primary void occurs. This critical point could be interpreted as the coalescence of secondary voids,

which subsequently results in the linking of neighbouring primary voids. A shift between these two mechanisms occurs rather gradually as l_1 is increased. The same holds true for a stress triaxiality equal to 2.0, but the sudden shift in f_p becomes less prominent as the primary void grows more uniformly and almost retains its initial spherical shape, see Fig. 6 (b).

Fig. 7 (a) shows the evolution of the volume average secondary porosity f_s as the unit cell deforms. It is observed that f_s grows much faster with straining when the intrinsic material length is smaller than the secondary void size a_0, i.e., a_0/l_1 is larger than unity. Moreover, a sudden shift in the evolution of f_s occurs at the onset of coalescence in these cases, which is directly related to rapid void growth inside the inter-void ligament material, as previously observed in Fig. 6. This shift is not as visible for $l_1 = 0.05$ μm as only minimal secondary void growth occurs.

To evaluate the contribution to the overall porosity from the secondary voids, the ratio between the volume average secondary porosity f_s and the total porosity f_{tot} is given in Fig. 7 (b). A negative slope indicates that the overall porosity growth is dominated by the growth of the primary voids, while a positive slope implies that the overall porosity growth is dominated by the growth of the secondary voids. It is seen that the slope gradually shifts from negative to positive as l_1 is decreased, which is true for both stress triaxialities. In all cases, except for $l_1 = 0.05$ μm, an abrupt increase in the slope occurs after the point of coalescence which indicates that the growth of secondary voids dominates in this phase. Whether this accelerated growth of secondary voids occurs or not, indicates the main mechanism of failure previously discussed.

5.3. Ductility

Ductility can be quantified by the strain at which coalescence occurs, if fracture occurs shortly after the material loses its load-carrying capacity. The critical macroscopic strain at coalescence E_{cr} is given as a function of the stress triaxiality in Fig. 8. The exponential decrease in ductility with increasing stress triaxiality can be immediately recognized. The value of E_{cr} is almost halved when the Gurson-Tvergaard model is used for the matrix material instead of von Mises plasticity. A gradual rise in ductility occurs when the intrinsic material length l_1 is increased. However, l_1 must be rather small compared to the size of the secondary population of voids to observe any significant contribution from them on the ductility.

5.4. Inter-void ligament width

The predicted width of the ligament material between primary voids in the $x_2 x_3$-plane at the strain level given in Fig. 6 (a) is illustrated in Fig. 9 and compared to an SEM image of the fracture surface of the AA6110 alloy (Thomesen et al., 2020). The figures are scaled to the same size for comparison. The fractography is taken from an axisymmetric specimen with a notch radius of 2 mm. The stress triaxiality in the centre of such a specimen is expected to be approximately 1.1-1.3 during plastic deformation in tension. The fracture surface consists of large dimples, associated with constituent particles, and some small areas with a high density of small dimples. The spacing between the larger dimples is not as large as predicted with the Gurson-Tvergaard model. Indeed, the initial size of the dispersoids a_0 must be in the same range as the intrinsic material length l_1 for a reasonable representation of the fracture surface.

5.5. Influence of deviatoric loading

The deviatoric stress state is also important for the damage evolution of ductile materials, especially at low stress triaxialities (Barsoum and Faleskog, 2007). Fig. 5 (c) and (e) display the macroscopic equivalent stress-strain curves of the unit cell for generalized shear ($L = 0$) and generalized compression ($L = 1$), respectively. As for generalized tension ($L = -1$) in Fig. 5 (a), the equivalent macroscopic stress is strongly reduced at the higher stress triaxiality because of the rapid expansion of the primary void. A minor
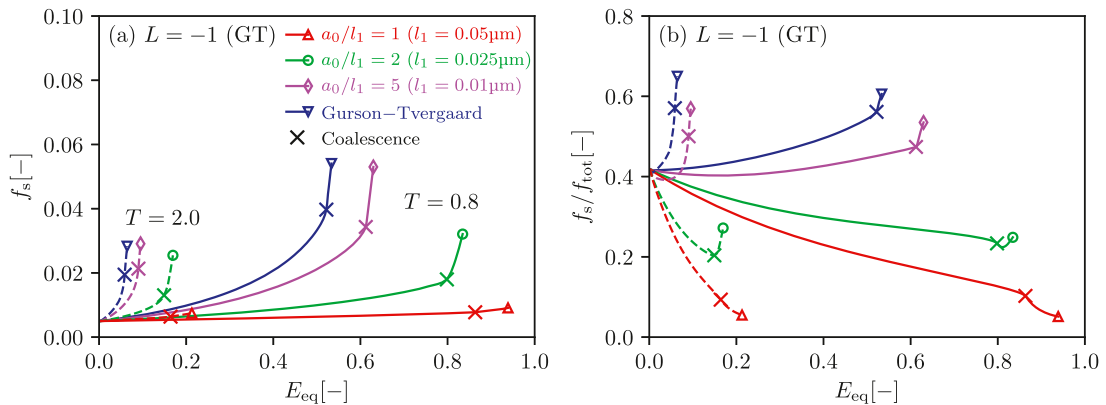

Fig. 7. (a) The volume average porosity f_s of secondary voids and (b) the ratio f_s/f_{tot} as a function of the macroscopic equivalent strain E_{eq} for a triaxiality of 0.8 (solid lines) and 2.0 (dashed lines). The point of coalescence is indicated by a cross (×). The simulations with von Mises plasticity governing the matrix material behaviour are not included as $f_s = 0$.
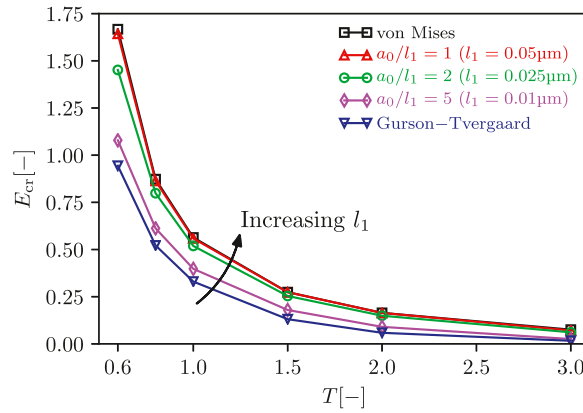
Fig. 8. Critical strain E_{cr} at coalescence (marked by a cross ($\times$) in Figs. 5 and 7) for $T \in [0.6,\ 3.0]$ and $L = -1$. The colour on the curves indicates the model used for the matrix material.
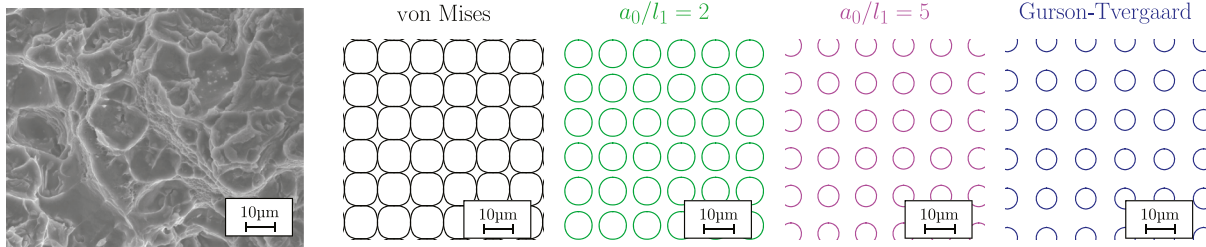

Fig. 9. The spacing between voids in the inter-void ligament ($x_2 x_3$-plane) at the strain level given in Fig. 6 (a) for $T = 0.8$ compared to an SEM image of the fracture surface of a notched axisymmetric tensile specimen of the AA6110 alloy, leftmost figure (Thomesen et al., 2020). Periodic distribution of voids is assumed.

increase in the equivalent macroscopic stress can be observed for generalized shear compared to generalized tension. We can still identify a distinct point of void coalescence where the deformation proceeds in a uniaxial deformation mode and leads to accelerated softening. In the case of generalized compression, the shift into a uniaxial deformation mode with the associated accelerated softening is absent, and void coalescence, as defined here, does not occur. In the case of a porous matrix material, the cell simulation terminates due to loss of load-carrying capacity in the integration point closest to the void surface as $f = q_1^{-1}$. It is interesting to notice that the influence of the matrix material model on the macroscopic stress response scales rather consistently with the changes in stress triaxiality and Lode parameter.

Fig. 5 (d) and (f) display the porosity of the primary void f_p for generalized shear and generalized compression, respectively. The growth of the primary void is fastest for generalized tension ($L = -1$) in Fig. 5 (b), intermediate for generalized shear ($L = 0$) and slowest for generalized compression ($L = 1$), i.e., the void growth rate decreases with increasing value of the Lode parameter. Similar results have been reported in other unit cell studies, e.g. Dæhli et al. (2018). As for generalized tension, the growth of the primary void with straining is initially the same for all constitutive models of matrix material and deviations are only seen at the onset of accelerated softening. As accelerated softening does not occur for generalized compression, the growth rate of the primary void remains the same until failure occurs due to excessive growth of the secondary voids.

The significance of the Lode parameter on the unit cell response, and particular the void growth, is linked to the evolution of the void shape (Dæhli et al., 2018). The contour of the primary void at peak equivalent macroscopic stress (marked by a circle ($\bullet$) in Fig. 5 (a)(c)(e)) in the three principal planes is plotted in Fig. 10 for generalized tension, generalized shear and generalized compression for stress triaxiality $T = 0.8,\ 1.0$ and 2.0. The different planes are identified by distinct colours. Solid lines represent a von Mises matrix material, while dashed lines indicate a Gurson-Tvergaard matrix material. The primary void evolves into a prolate shape for generalized tension and an oblate shape for generalized compression. The effect of the deviatoric stress state on void shape is more prominent at low stress triaxialities, and as the stress triaxiality increases, the effect fades out. The matrix material model only influences the size of the primary void and not its shape. This finding is rather obvious as the peak equivalent macroscopic stress occurs at a lower macroscopic equivalent strain for lower values of the intrinsic material length l_1 and the growth of the primary void has been shown to be largely unaffected by the existence of the secondary voids.

Fig. 11 displays histograms of the secondary porosity distribution within all integration points of the unit cell at peak equivalent macroscopic stress. Each bar in the plot represents the percentage of integration points with secondary porosity f within a given interval. Results are included for two values of the intrinsic material length l_1 in addition to the Gurson-Tvergaard model ($l_1 \to 0$). An
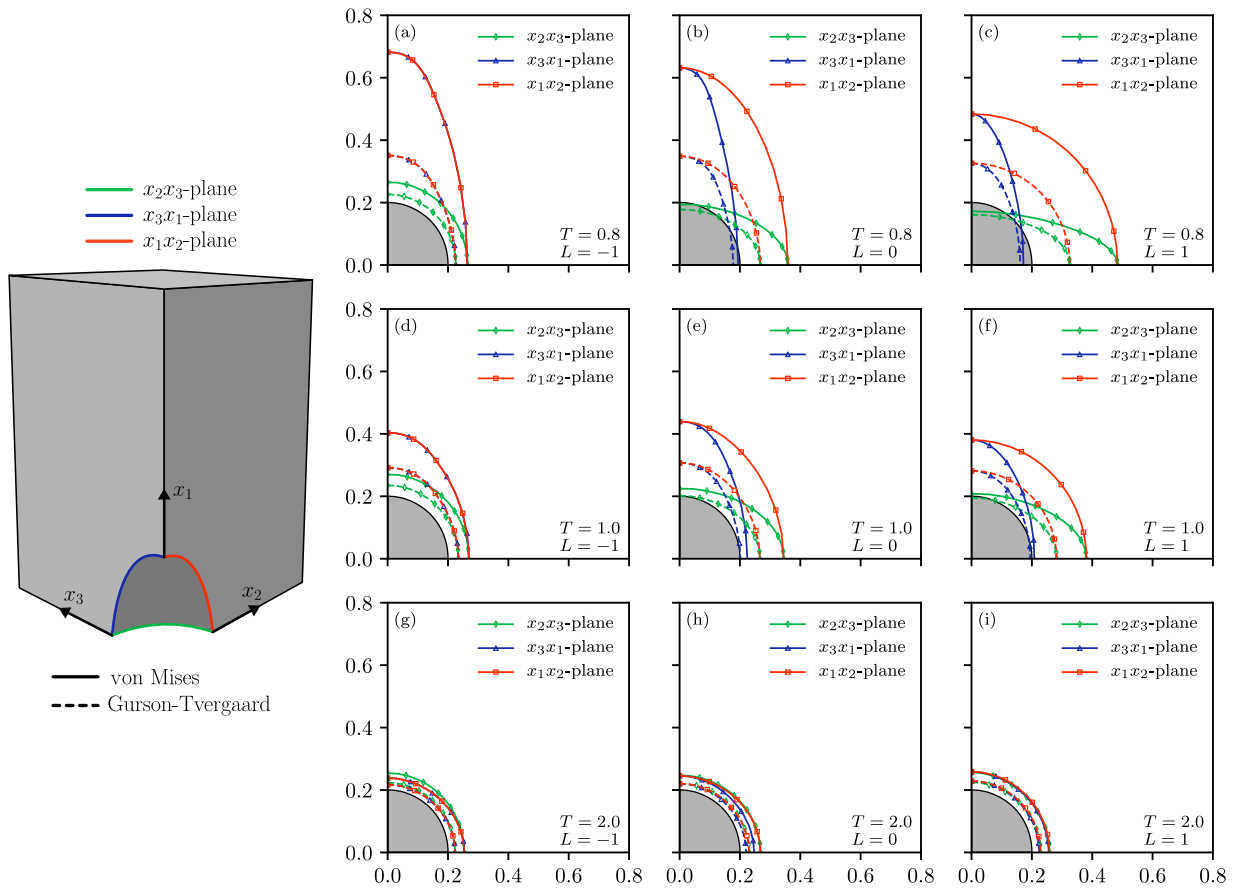
Fig. 10. The contours of the primary void in the x_ix_j-plane at peak equivalent macroscopic stress (marked by a circle (●) in Fig. 5(a)(c)(e)) for different combinations of stress triaxiality and Lode parameter. The void radii on the vertical and horizontal axes are in μm. The shaded circle with centre in the origin represents the initial spherical void. The red, blue and green curves correspond to the x_1x_2-plane, x_3x_1-plane and x_2x_3-plane, respectively. Solid and dashed lines represent simulations with von Mises plasticity and the Gurson-Tvergaard model, respectively.

increase in both mean value and spread of secondary porosity f arises as the value of l_1 is reduced. The same trend is recognized for decreasing overall stress triaxiality. This latter finding seems contradictory as the average microscopic stress triaxiality in the matrix will decrease with the overall macroscopic stress triaxiality. However, the microscopic plastic strain in the integration points is in general higher as slower growth of the primary void allows for larger deformation of the cell at peak equivalent stress. The secondary porosity distributions for generalized tension and generalized shear are rather comparable, whereas for generalized compression the mean value is higher and the spread lower within the unit cell.

6. Concluding remarks

Finite-element based unit cell simulations of a primary void embedded in a matrix material governed by the size-dependent Monchiet-Bonnet porous plasticity model were conducted to disclose the effect of secondary voids on ductile fracture. The primary voids are assumed nucleated on the constituent particles in an aluminium alloy, whereas the secondary voids are assumed nucleated on dispersoids, which are typically one order of magnitude smaller than the constituent particles. By letting the intrinsic material length l_1 of the Monchiet-Bonnet model tend to zero, the Gurson-Tvergaard model is obtained, while as the intrinsic material length tends to infinity, the material becomes isochoric and governed by a pressure-insensitive yield criterion similar to the von Mises yield criterion. Simulations were performed to study the influence of the intrinsic material length scale and the imposed stress state on the macroscopic response and ductility of the unit cell.

By adopting the Gurson-Tvergaard model for the matrix material, the change in the overall response and ductility of the unit cell is considerable and induced by the weakening of the material in the inter-void ligament due to extensive growth of secondary voids. However, the width of the material surrounding the large dimples at fracture does not compare well to the fracture surface from physical tests, suggesting that a non-zero intrinsic material length l_1 should be introduced to account for void size effects.

The unit cell simulations with the Monchiet-Bonnet model for the matrix material demonstrates that the intrinsic material length scale must be in the same range as the size of the dispersoids or even smaller for the secondary voids to grow substantially and thereby affect the overall response and ductility of the unit cell. As the initial ratio a_0/l_1 increases, the coalescence mode gradually progresses
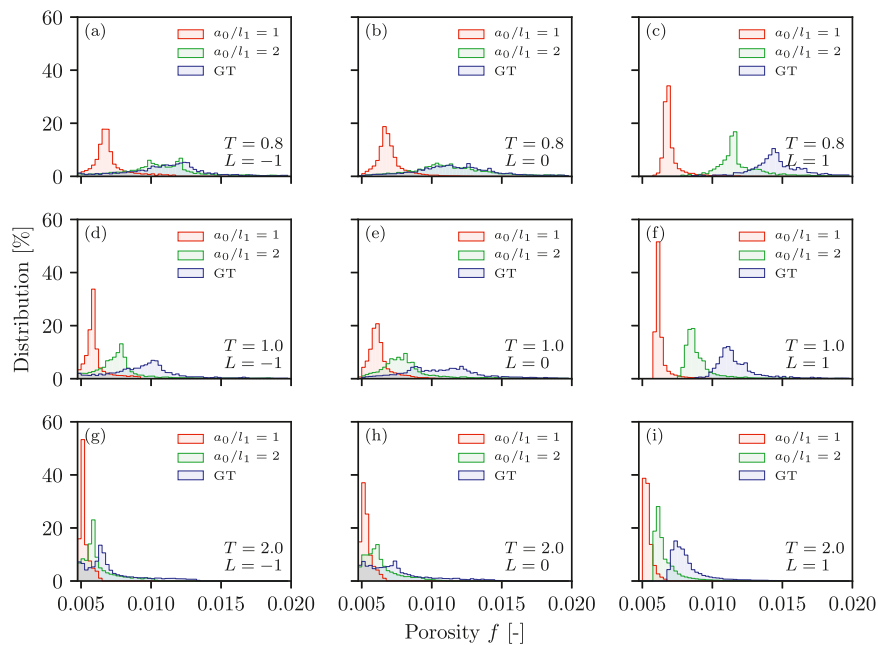
Fig. 11. Histograms of the distribution of the secondary porosity f within all integration points of the unit cell at peak equivalent macroscopic stress. The interval size of the bars is 0.00025, where each bar represents the percentage of integration points with f within this interval. Red, green and blue coloured bars correspond to different material models for the matrix material and the same colour code as in previous graphs is applied.

from internal necking, as obtained with von Mises plasticity in the matrix, to a total loss of strength in the inter-void ligament material. The presence of the secondary voids has no influence on the initial growth of the primary void but promotes earlier void coalescence in generalized tension and generalized shear and thus decreases the ductility. The effect of the secondary voids on void coalescence and ductility is controlled by the ratio a_0/l_1. In generalized compression, void coalescence does not occur, and failure occurs exclusively by excessive growth of the secondary voids.

Comparison of the predicted spacing between voids at failure with an SEM image of the fracture surface of a notched axisymmetric tensile specimen of the AA6110 alloy indicates that the intrinsic material length should be in the range of the size of the dispersoids. An intrinsic material length of 0.1 μm is in the very limit of what has been proposed in the literature (Hutchinson, 2000; Evans and Hutchinson, 2009) which might indicate that the dispersoids have rather limited effect on the ductility of the AA6110 alloy. However, the intrinsic material length at which size effects start to contribute is not exactly known and is probably dependent on the material. In these simulations, it was assumed that the secondary voids were nucleated on the dispersoids from the start. It is known from the literature that voids nucleate less readily on small particles than on large ones, which implies that this assumption will lead to an overestimation of the effect of the dispersoids on ductile failure. From these considerations, it is expected that the influence of dispersoids on ductile failure in aluminium alloys is limited.

CrediT Author Statement

Declaration of Competing Interest

Acknowledgement

References

Alves, M., Jones, N., 1999. Influence of hydrostatic stress on failure of axisymmetric notched specimens. J. Mech. Phys. Solids 47, 643–667. https://doi.org/10.1016/S0022-5096(98)00060-X.

Ashby, M.F., 1970. The deformation of plastically non-homogeneous materials. Philos. Mag. A J. Theor. Exp. Appl. Phys. 21, 399–424. https://doi.org/10.1080/14786437008238426.

Bao, Y., Wierzbicki, T., 2004. On fracture locus in the equivalent strain and stress triaxiality space. Int. J. Mech. Sci. 46, 81–98. https://doi.org/10.1016/j.ijmecsci.2004.02.006.

Barsoum, I., Faleskog, J., 2007. Rupture mechanisms in combined tension and shear-Experiments. Int. J. Solids Struct. 44, 1768–1786. https://doi.org/10.1016/j.ijsolstr.2006.09.031.

Barsoum, I., Faleskog, J., 2011. Micromechanical analysis on the influence of the Lode parameter on void growth and coalescence. Int. J. Solids Struct. 48, 925–938. https://doi.org/10.1016/j.ijsolstr.2010.11.028.

Belytschko, T., Liu, W.K., Moran, B., Elkhodary, K.I., 2014. Nonlinear Finite Elements for Continua and Structures, 2nd ed. Wiley.

Benzerga, A.A., Leblond, J.-B., 2010. Ductile Fracture by Void Growth to Coalescence. Adv. Appl. Mech. 44, 169–305. https://doi.org/10.1016/S0065-2156(10)44003-X.

Broek, D., 1973. The role of inclusions in ductile fracture and fracture toughness. Eng. Fract. Mech. 5, 55–66. https://doi.org/10.1016/0013-7944(73)90007-6.

Campbell, J., 2011. The origin of griffith cracks. Metall. Mater. Trans. B. 42, 1091–1097. https://doi.org/10.1007/s11663-011-9575-5.

Chu, C.C., Needleman, A., 1980. Void Nucleation Effects in Biaxially Stretched Sheets. J. Eng. Mater. Technol. 102, 249–256. https://doi.org/10.1115/1.3224807.

Cox, T.B., Low, J.R., 1974. An investigation of the plastic fracture of AISI 4340 and 18 Nickel-200 grade maraging steels. Metall. Trans. 5, 1457–1470. https://doi.org/10.1007/BF02646633.

Dæhli, L.E.B., Faleskog, J., Børvik, T., Hopperstad, O.S., 2017. Unit cell simulations and porous plasticity modelling for strongly anisotropic FCC metals. Eur. J. Mech. -A/Solids 65, 360–383. https://doi.org/10.1016/j.euromechsol.2017.05.004.

Dæhli, L.E.B., Morin, D., Børvik, T., Hopperstad, O.S., 2018. A Lode-dependent Gurson model motivated by unit cell analyses. Eng. Fract. Mech. 190, 299–318. https://doi.org/10.1016/j.engfracmech.2017.12.023.

Dons, A.L., 2001. The Alstruc homogenization model for industrial aluminum alloys. J. Light Met. 1, 133–149. https://doi.org/10.1016/S1471-5317(01)00007-4.

Dunand, M., Mohr, D., 2011. On the predictive capabilities of the shear modified Gurson and the modified Mohr-Coulomb fracture models over a wide range of stress triaxialities and Lode angles. J. Mech. Phys. Solids 59, 1374–1394. https://doi.org/10.1016/j.jmps.2011.04.006.

El-Magd, E., Brodmann, M., 2001. Influence of precipitates on ductile fracture of aluminium alloy AA7075 at high strain rates. Mater. Sci. Eng. A 307, 143–150. https://doi.org/10.1016/S0921-5093(00)01961-4.

Erice, B., Roth, C.C., Mohr, D., 2018. Stress-state and strain-rate dependent ductile fracture of dual and complex phase steel. Mech. Mater. 116, 11–32. https://doi.org/10.1016/j.mechmat.2017.07.020.

Evans, A.G., Hutchinson, J.W., 2009. A critical assessment of theories of strain gradient plasticity. Acta Mater 57, 1675–1688. https://doi.org/10.1016/j.actamat.2008.12.012.

Fabrègue, D., Pardoen, T., 2008. A constitutive model for elastoplastic solids containing primary and secondary voids. J. Mech. Phys. Solids 56, 719–741. https://doi.org/10.1016/j.jmps.2007.07.008.

Faleskog, J., Shih, C.F., 1997. Micromechanics of coalescence - I. Synergistic effects of elasticity, plastic yielding and multi-size-scale voids. J. Mech. Phys. Solids 45, 21–25. https://doi.org/10.1016/S0022-5096(96)00078-6.

Faleskog, J., Barsoum, I., 2013. Tension-torsion fracture experiments - Part I: Experiments and a procedure to evaluate the equivalent plastic strain. Int. J. Solids Struct. 50, 4241–4257. https://doi.org/10.1016/j.ijsolstr.2013.08.029.

Fleck, N.A., Muller, G.M., Ashby, M.F., Hutchinson, J.W., 1994. Strain gradient plasticity: Theory and experiment. Acta Metall. Mater. 42, 475–487. https://doi.org/10.1016/0956-7151(94)90502-9.

Fleck, N.A., Hutchinson, J.W., 1997. Strain Gradient Plasticity. Adv. Appl. Mech. 33, 295–361. https://doi.org/10.1016/S0065-2156(08)70388-0.

Gao, H., Huang, Y., Nix, W.D., 1999. Modeling plasticity at the micrometer scale. Naturwissenschaften 86, 507–515. https://doi.org/10.1007/s001140050665.

Gao, X., Zhang, T., Hayden, M., Roe, C., 2009. Effects of the stress state on plasticity and ductile failure of an aluminum 5083 alloy. Int. J. Plast. 25, 2366–2382. https://doi.org/10.1016/j.ijplas.2009.03.006.

Gruben, G., Hopperstad, O.S., Børvik, T., 2012. Evaluation of uncoupled ductile fracture criteria for the dual-phase steel Docol 600DL. Int. J. Mech. Sci. 62, 133–146. https://doi.org/10.1016/j.ijmecsci.2012.06.009.

Gurson, A.L., 1977. Continuum Theory of Ductile Rupture by Void Nucleation and Growth: Part I—Yield Criteria and Flow Rules for Porous Ductile Media. J. Eng. Mater. Technol. 99, 2–15. https://doi.org/10.1115/1.3443401.

Hahn, G.T., Rosenfield, A.R., 1975. Metallurgical factors affecting fracture toughness of aluminum alloys. Metall. Trans. A 6, 653–668. https://doi.org/10.1007/BF02672285.

Haltom, S.S., Kyriakides, S., Ravi-Chandar, K., 2013. Ductile failure under combined shear and tension. Int. J. Solids Struct. 50, 1507–1522. https://doi.org/10.1016/j.ijsolstr.2012.12.009.

Hannard, F., Pardoen, T., Maire, E., Le Bourlot, C., Mokso, R., Simar, A., 2016. Characterization and micromechanical modelling of microstructural heterogeneity effects on ductile fracture of 6xxx aluminium alloys. Acta Mater 103, 558–572. https://doi.org/10.1016/j.actamat.2015.10.008.

Hill, R., 1967. The essential structure of constitutive laws for metal composites and polycrystals. J. Mech. Phys. Solids 15, 79–95. https://doi.org/10.1016/0022-5096(67)90018-X.

Huang, Y., Gao, H., Nix, W.D., Hutchinson, J.W., 2000. Mechanism-based strain gradient plasticity - II. Analysis. J. Mech. Phys. Solids 48, 99–128. https://doi.org/10.1016/S0022-5096(99)00022-8.

Hutchinson, J.W., 2000. Plasticity at the micron scale. Int. J. Solids Struct. 37, 225–238. https://doi.org/10.1016/S0020-7683(99)00090-6.

Johnson, G.R., Cook, W.H., 1985. Fracture characteristics of three metals subjected to various strains, strain rates, temperatures and pressures. Eng. Fract. Mech. 21, 31–48. https://doi.org/10.1016/0013-7944(85)90052-9.

Koplik, J., Needleman, A., 1988. Void growth and coalescence in porous plastic solids. Int. J. Solids Struct. 24, 835–853. https://doi.org/10.1016/0020-7683(88)90051-0.

Li, Z., Huang, M., Wang, C., 2003. Scale-dependent plasticity potential of porous materials and void growth. Int. J. Solids Struct. 40, 3935–3954. https://doi.org/10.1016/S0020-7683(03)00178-1.

Li, Z., Huang, M., 2005. Combined effects of void shape and void size - Oblate spheroidal microvoid embedded in infinite non-linear solid. Int. J. Plast. 21, 625–650. https://doi.org/10.1016/j.ijplas.2004.05.006.

Ma, Q., Clarke, D.R., 1995. Size dependent hardness of silver single crystals. J. Mater. Res. 10, 853–863. https://doi.org/10.1557/JMR.1995.0853.

Maire, E., Zhou, S., Adrien, J., Dimichiel, M., 2011. Damage quantification in aluminium alloys using in situ tensile tests in X-ray tomography. Eng. Fract. Mech. 78, 2679–2690. https://doi.org/10.1016/j.engfracmech.2011.07.004.

Mandel, J., 1966. Contribution théorique à l'étude de l'écrouissage et des lois de l'écoulement plastique. In: Görtler, H. (Ed.), Appl. Mech. Springer, Berlin, Heidelb, pp. 502–509. https://doi.org/10.1007/978-3-662-29364-5_67.

McClintock, F.A., 1968. A Criterion for Ductile Fracture by the Growth of Holes. J. Appl. Mech. 35, 363–371. https://doi.org/10.1115/1.3601204.

Mirza, M.S., Barton, D.C., Church, P., 1996. The effect of stress triaxiality and strain-rate on the fracture characteristics of ductile metals. J. Mater. Sci. 31, 453–461. https://doi.org/10.1007/BF01139164.

Monchiet, V., Bonnet, G., 2013. A Gurson-type model accounting for void size effects. Int. J. Solids Struct. 50, 320–327. https://doi.org/10.1016/j.ijsolstr.2012.09.005.

Nahshon, K., Hutchinson, J.W., 2008. Modification of the Gurson Model for shear failure. Eur. J. Mech. A/Solids 27, 1–17. https://doi.org/10.1016/j.euromechsol.2007.08.002.

Needleman, A., Tvergaard, V., 1984. An analysis of ductile rupture in notched bars. J. Mech. Phys. Solids 32, 461–490. https://doi.org/10.1016/0022-5096(84)90031-0.

Nielsen, K.L., Tvergaard, V., 2011. Failure by void coalescence in metallic materials containing primary and secondary voids subject to intense shearing. Int. J. Solids Struct. 48, 1255–1267. https://doi.org/10.1016/j.ijsolstr.2011.01.008.

Niordson, C.F., Tvergaard, V., 2019. A homogenized model for size-effects in porous metals. J. Mech. Phys. Solids 123, 222–233. https://doi.org/10.1016/j.jmps.2018.09.004.

Nix, W.D., Gao, H., 1998. Indentation size effects in crystalline materials: A law for strain gradient plasticity. J. Mech. Phys. Solids 46, 411–425. https://doi.org/10.1016/S0022-5096(97)00086-0.

Ortiz, M., Simo, J.C., 1986. An analysis of a new class of integration algorithms for elastoplastic constitutive relations. Int. J. Numer. Methods Eng. 23, 353–366. https://doi.org/10.1002/nme.1620230303.

Pardoen, T., Hutchinson, J.W., 2000. An extended model for void growth and coalescence. J. Mech. Phys. Solids 48, 2467–2512. https://doi.org/10.1016/S0022-5096(00)00019-3.

Pedersen, K.O., Westermann, I., Furu, T., Børvik, T., Hopperstad, O.S., 2015. Influence of microstructure on work-hardening and ductile fracture of aluminium alloys. Mater. Des. 70, 31–44. https://doi.org/10.1016/j.matdes.2014.12.035.

Pineau, A., Benzerga, A.A., Pardoen, T., 2016. Failure of metals I: Brittle and ductile fracture. Acta Mater 107, 424–483. https://doi.org/10.1016/j.actamat.2015.12.034.

Poole, W.J., Ashby, M.F., Fleck, N.A., 1996. Micro-hardness of annealed and work-hardened copper polycrystals. Scr. Mater. 34, 559–564. https://doi.org/10.1016/1359-6462(95)00524-2.

Rice, J.R., Tracey, D.M., 1969. On the ductile enlargement of voids in triaxial stress fields. J. Mech. Phys. Solids 17, 201–217. https://doi.org/10.1016/0022-5096(69)90033-7.

Scales, M., Tardif, N., Kyriakides, S., 2016. Ductile failure of aluminum alloy tubes under combined torsion and tension. Int. J. Solids Struct. 97–98, 116–128. https://doi.org/10.1016/j.ijsolstr.2016.07.038.

Simo, J.C., Hughes, T.J.R., 1998. Computational Inelasticity. Springer-Verlag.

Stelmashenko, N.A., Walls, M.G., Brown, L.M., Milman, Y.V., 1993. Microindentations on W and Mo oriented single crystals: An STM study. Acta Metall. Mater. 41, 2855–2865. https://doi.org/10.1016/0956-7151(93)90100-7.

Stölken, J.S., Evans, A.G., 1998. A microbend test method for measuring the plasticity length scale. Acta Mater 46, 5109–5115. https://doi.org/10.1016/S1359-6454(98)00153-0.

Thomesen, S., 2019. Plastic flow and fracture of isotropic and anisotropic 6000-series aluminium alloys: experiments and numerical simulations. Norwegian University of Science and Technology. PhD thesis.

Thomesen, S., Hopperstad, O.S., Myhr, O.R., Børvik, T., 2020. Influence of stress state on plastic flow and ductile fracture of three 6000-series aluminium alloys. Mater. Sci. Eng. A 783, 139295 https://doi.org/10.1016/j.msea.2020.139295.

Toda, H., Oogo, H., Horikawa, K., Uesugi, K., Takeuchi, A., Suzuki, Y., Nakazawa, M., Aoki, Y., Kobayashi, M., 2014. The True Origin of Ductile Fracture in Aluminum Alloys. Metall. Mater. Trans. A. 45, 765–776. https://doi.org/10.1007/s11661-013-2013-3.

Tvergaard, V., 1981. Influence of voids on shear band instabilities under plane strain conditions. Int. J. Fract. 17, 389–407. https://doi.org/10.1007/BF00036191.

Tvergaard, V., 1982. On localization in ductile materials containing spherical voids. Int. J. Fract. 18, 237–252. https://doi.org/10.1007/BF00015686.

Tvergaard, V., Needleman, A., 1984. Analysis of the Cup-Cone Fracture in a Round Tensile Bar. Acta Metall 32, 157–169. https://doi.org/10.1016/0001-6160(84)90213-X.

Tvergaard, V., 1998. Interaction of very small voids with larger voids. Int. J. Solids Struct. 35, 3989–4000. https://doi.org/10.1016/S0020-7683(97)00254-0.

Underwood, E.E., 1970. Quantitative Stereology. Addison-Wesley Pub. Co, Reading, Mass.

Wen, J., Huang, Y., Hwang, K.C., Liu, C., Li, M., 2005. The modified Gurson model accounting for the void size effect. Int. J. Plast. 21, 381–395. https://doi.org/10.1016/j.ijplas.2004.01.004.

Westermann, I., Pedersen, K.O., Furu, T., Børvik, T., Hopperstad, O.S., 2014. Effects of particles and solutes on strength, work-hardening and ductile fracture of aluminium alloys. Mech. Mater. 79, 58–72. https://doi.org/10.1016/j.mechmat.2014.08.006.